

Solar Energy Utilization

International Edition: DOI: 10.1002/anie.201810694

German Edition: DOI: 10.1002/ange.201810694



Disorder Engineering in Monolayer Nanosheets Enabling Photothermic Catalysis for Full Solar Spectrum (250–2500 nm) Harvesting

Min-Quan Yang, Lei Shen, Yuyao Lu, See Wee Chee, Xin Lu, Xiao Chi, Zhihui Chen, Qing-Hua Xu, Utkur Mirsaidov, and Ghim Wei Ho*

Abstract: A persistent challenge in classical photocatalyst systems with extended light absorption is the unavoidable trade-off between maximizing light harvesting and sustaining high photoredox capability. Alternatively, cooperative energy conversion through photothermic activation and photocatalytic redox is a promising yet unmet scientific proposition that critically demands a spectrum-tailored catalyst system. Here, we construct a solar thermal-promoted photocatalyst, an ultrathin “biphasic” ordered–disordered D-HNb₃O₈ junction, which performs two disparate spectral selective functions of photoexcitation by ordered structure and thermal activated conversion via disordered lattice for combinatorial photo-thermal mediated catalysis. This *in situ* synthetically immobilized lattice distortion, constrained to a single-entity monolayer structure not only circumvents interfacial incompatibility but also triggers near-field temperature rise at the catalyst–reactant complexes’ proximity to promote photoreaction. Ultimately, a generic full solar conversion improvement for H₂ fuel production, organic transformation and water purification is realized.

Improving solar energy utilization is a key yet challenging proposition in photocatalysis, which dominates sustainable solar-to-chemical energy conversion.^[1] To maximize solar energy capture, a photocatalyst system that harvests the

entire range of solar spectrum is necessary.^[1b] Over the past decades, the continual search of such photocatalyst has led to extensive developments in the designing and engineering of photoactive nanomaterials. Diverse strategies such as band-gap engineering,^[2] sensitization,^[3] upconversion^[1b,4] and hetero-structure constructing^[5] have been devised. However, the realization of total solar spectrum (250–2500 nm) absorption for efficient photoredox still remains scarce. A critical bottleneck over these strategies is the difficulty in realizing full light capture and maintaining suitable redox potentials of photogenerated charge carriers for triggering chemical reactions.^[1b,6] Moreover, the side effects such as insufficient charge carrier separation arising from the small band gap, or the low yield of energetic charge carriers originating from the narrow light absorption band^[1b] also immensely hinder the solar energy conversion efficiency of current wide-spectrum-response photocatalyst systems.

In view of these constraints, the recent overture of photothermally accelerated catalysis provides an alternative avenue to promote the solar energy utilization.^[1b] Different from the traditional approaches of utilizing extended light absorption to generate charge carriers, the photothermal catalysis dissipates the absorbed photon energy into heat to accelerate photocatalytic reaction. It is theoretically able to fully utilize the solar energy. However, the energy conversion efficiency at present is still deemed poor owing to some material and structure constraints which undeniably dictate some drawbacks such as i) relatively narrow range of light absorption and/or low absorption coefficient of photothermic materials, e.g., surface plasmon resonance metals heater; ii) low content of the photothermic material in the composite system (generally below 10 wt.%) resulted from the disparate function competition between the photoexcitation and photothermal activation components; iii) interfacial energy loss at photothermal and photoredox active intersection. In this context, developing an integral, unitary catalyst system that directly facilitates two distinct undertakings of high photoredox and efficient photothermic conversion for the full solar light conversion is highly sought after.

Here, we fabricate a single-entity ordered-disordered HNb₃O₈ monolayer structure (D-HNb₃O₈) via a room temperature reduction, termed “solar thermal-promoted photocatalyst”, tailored to efficiently perform simultaneous photoredox and photoheating at respective optimal working spectrum. The D-HNb₃O₈ monolayer consists of two phases: crystalline domains and highly disordered “nano-islands” where the atomically engineered defects reside

[*] Dr. M.-Q. Yang, Y. Lu, X. Lu, Prof. G. W. Ho
Department of Electrical and Computer Engineering
National University of Singapore
117583, Singapore (Singapore)
E-mail: elehw@nus.edu.sg

Dr. L. Shen
Department of Mechanical Engineering
National University of Singapore
117575, Singapore (Singapore)

Dr. S. W. Chee, Prof. U. Mirsaidov
Department of Physics, National University of Singapore
117551, Singapore (Singapore)

Dr. X. Chi
Singapore Synchrotron Light Source
National University of Singapore
117603, Singapore (Singapore)

Dr. Z. Chen, Prof. Q.-H. Xu
Department of Chemistry, National University of Singapore
117543, Singapore (Singapore)

 Supporting information and the ORCID identification number(s) for the author(s) of this article can be found under <https://doi.org/10.1002/anie.201810694>.

locally within the crystalline lattice. Such structure retains the benefits of crystalline regions for photocatalytic reaction, while the lattice disorders yield new gap states that induce full solar absorption with ca. 80% average absorbance for photoheating. Besides, coordinating ordered-disordered phases-on-ultrathin sheet brings about the required high surface reactivity and shortens the transport length to the atomic scale dimensions. Consequently, the D-HNb₃O₈ exhibits a universal photochemical activities enhancement under full spectrum irradiation toward H₂ production, reductive organic transformation and oxidative dye degradation beyond the limitation of UV light excitation. This work denotes a viable approach for full solar energy capture by photothermal catalysis using a single entity of designed catalyst system, which is realized via a facile disorder engineering method that bypasses excessive energy input and manipulation complexity constraints.

The monolayer HNb₃O₈ nanosheets (HNb₃O₈ ns) were prepared from cation-exchange assisted exfoliation process (Figure S1–S7 in the Supporting Information).^[7] Subsequently, disorder engineering of HNb₃O₈ was carried out via a facile room temperature reduction over deposited Pd. Active H species [H_s] are spontaneously dissociated on the Pd surface owing to its strong dissociation ability of H₂.^[8] The generated [H_s] are highly reductive and react with the monolayer HNb₃O₈ lattice to generate localized disorder (Figure 1a). This leads to a highly accessible approach

towards low temperature creation of abundant defects on crystalline lattice, thus forming the ordered-disordered D-HNb₃O₈.

Figure 1b shows the scanning electron microscopy (SEM) image of the disorder-rich D-HNb₃O₈, which reveals a uniform nanosheet morphology. Energy dispersive X-ray spectroscopy (EDS) analysis shows that Pd is dispersed throughout the nanosheet (Figure S8). Atomic force microscopy (AFM) analysis determines that the average sheet thickness of D-HNb₃O₈ is about 1.2 nm (Figure 1c,d), indicating atomically thin monolayer HNb₃O₈ along the [010] direction (Figure S9).^[7] The thickness is the same as that of the pristine HNb₃O₈ (Figure S7). This implies that the mild disorder engineering at room temperature favorably preserves the morphology of the original HNb₃O₈. Figure 1e shows the Raman spectra of the D-HNb₃O₈ and HNb₃O₈ nanosheets. The significant weakening and broadening of all the Raman modes of D-HNb₃O₈ indicates a pronounced microstructural modification of the HNb₃O₈ after the room temperature reduction. This change is also verified by the X-ray diffraction (XRD) analysis where the D-HNb₃O₈ shows a decreased crystallinity with respect to pristine HNb₃O₈ (Figure S6).

Figure 1f and Figure S10–S12 show transmission electron microscopy (TEM) analysis of the D-HNb₃O₈ nanosheets (D-HNb₃O₈ ns), which shows that metallic Pd nanoparticles with an average diameter of 2–5.5 nm are well-dispersed on the ultrathin D-HNb₃O₈. Notably, the in situ synthetically localized lattice distortion can be readily visualized by the high-resolution TEM analysis (Figure 1g and Figure S13). The monolayer D-HNb₃O₈ nanosheet reveals coexistence of “two phases”: well-defined crystalline regions with distinct lattice fringes, and highly disordered “nanoislands” with distorted crystal lattice. This is markedly different from the pristine HNb₃O₈ that features high crystallinity and well-resolved lattice fringes (Figure S14). The common occurrence of the spatially localized lattice disorder on the monolayer D-HNb₃O₈ nanosheets confirms the effectiveness of the low temperature defects generation technique.

To validate the defect-rich nature of the D-HNb₃O₈, X-ray photoelectron spectroscopy (XPS) and electron paramagnetic resonance (EPR) analyses have been performed. For comparison, the pristine HNb₃O₈ is also analyzed. The survey XPS spectrum and high-resolution Pd spectrum^[9] of D-HNb₃O₈ further affirms the metallic nature of Pd (Figure S15a,b). More importantly, the D-HNb₃O₈ displays a significant oxygen vacancy (V_O) peak at 531.9 eV (Figure 1h),^[10] which is greatly larger than that of pristine HNb₃O₈ (Figure S15c). Meanwhile, the Nb 3d spectrum of D-HNb₃O₈ shows two new peaks of Nb⁴⁺ at 208.6 and 205.5 eV,^[11] which are absent in HNb₃O₈ (Figure S15d). Moreover, the EPR analysis of the D-HNb₃O₈ also displays strong signals of Nb⁴⁺ and V_O sites,^[12] while the pristine HNb₃O₈ only presents a very weak V_O peak and no Nb⁴⁺ signal is detected (Figure 2a). The collective XPS and EPR results reveal that the monolayer HNb₃O₈ nanosheet is highly reduced through the room temperature reduction process, which creates abundant V_O accompanied by partial reduction of the Nb⁵⁺ to Nb⁴⁺, thereby giving rise to an ordered-disordered D-HNb₃O₈ structure. In addition, the EPR signals at g values from 2.02 to 2.15 can be referred to

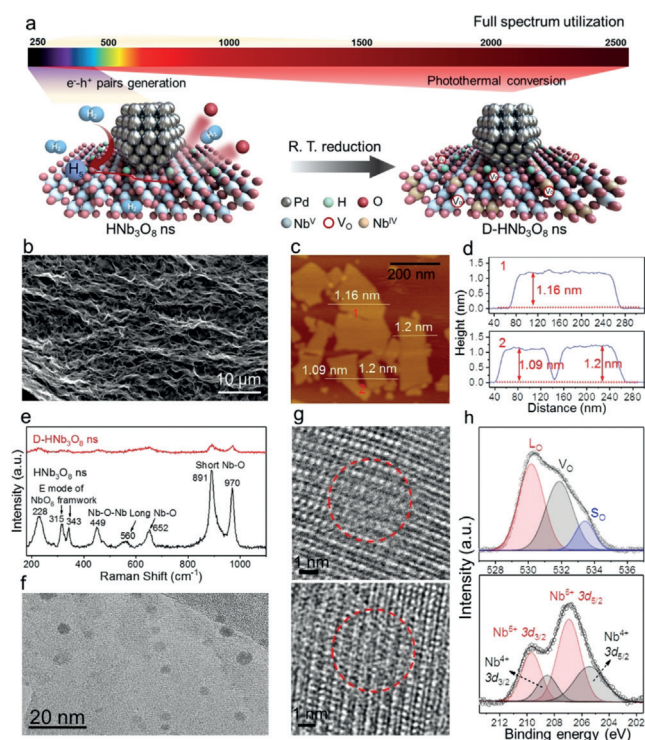


Figure 1. a) Schematic synthesis of disorder-rich D-HNb₃O₈. b) SEM image, c) AFM image, and d) corresponding height profiles of D-HNb₃O₈. e) Raman spectra of D-HNb₃O₈ and pristine HNb₃O₈. f) TEM, g) HRTEM, and h) XPS analysis of D-HNb₃O₈. Note: R.T. refers to room temperature. L₀, V₀ and S₀ are associated with lattice oxygen, oxygen vacancy and surface adsorbed water/hydroxyl groups, respectively.

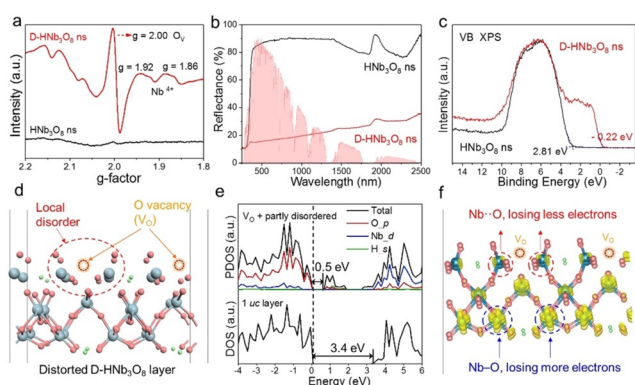


Figure 2. a) Low temperature EPR, b) UV-vis-NIR DRS spectra, and c) VB XPS of D-HfNb₃O₈ and pristine HfNb₃O₈. d–f) DFT calculation of D-HfNb₃O₈.

the superimposed signals of surface oxygen radical species and hole trapping states.^[13]

In view of the abundant lattice disorders in the D-HfNb₃O₈, an effective modulation of band gap and light harvesting property is expected.^[14] This has been visually verified by a drastic color change of the D-HfNb₃O₈ during reduction process (Figure S16). To accurately assess the optical properties, UV-vis-NIR diffuse reflectance spectroscopy (DRS) is employed. The pristine HfNb₃O₈ presents a sharp band-edge absorption at around 360 nm. The light absorption in the range above 360 nm is less than 10%. In contrast, D-HfNb₃O₈ features an excellent full light absorption with an average absorbance close to 80% (Figure 2b). Notably, a control sample of 1% Pd/HfNb₃O₈ nanosheets with the same weight content of Pd as that of the D-HfNb₃O₈ but less defect shows a much lower light absorption of ca. 35% in the visible-NIR region (Figure S17). This affirms that the strong visible-NIR light absorption of D-HfNb₃O₈ is induced by the Pd-induced disorder rather than the d–d transition of Pd nanoparticles. Moreover, the calculated band structures reveal that besides the typical HfNb₃O₈ band gap of 3.5 eV, another smaller band gap (<0.5 eV) appears in D-HfNb₃O₈ (Figure S18). Further valence band XPS (VB XPS) analysis (Figure 2c) of the D-HfNb₃O₈ shows two apparent bands at 2.81 and –0.22 eV below the Fermi energy, whereas the HfNb₃O₈ only presents a maximum energy edge at about 2.81 eV. These results consolidate that the high inclusion of lattice disorders within the crystalline structure induces new gap states in the D-HfNb₃O₈.

To further understand the band feature of D-HfNb₃O₈, density functional theory (DFT) based calculations are conducted (Figure 2d–f and Figure S19). The calculated total density of states (DOS) of the ordered HfNb₃O₈ layer (O_{2p} for VB maximum, Nb_{4d} for conduction band (CB) minimum) show a band gap energy of around 3.4 eV (Figure 2e), in good agreement with the experimental value of 3.5 eV. In comparison, the projected density of states (PDOS) of the D-HfNb₃O₈ validate that the V_O and the resulted structural disorder induces a mid-gap hybridized state of O_{2p} and H_{1s}, which narrows the band gap of D-HfNb₃O₈ to 0.5 eV. A 3D distribution of the partial charge density of the mid-gap state between 0.5 and 1.5 eV of the D-HfNb₃O₈

(Figure 2f) reveals that with the removal of O atoms, the neighboring Nb atoms in the disordered domain have a higher tendency to lose less electrons than those in the crystalline region, resulting in a reductive Nb oxidation state (Nb⁵⁺ to Nb⁴⁺) in the vicinity of the V_O. The finding is consistent with our XPS and EPR analyses. The combined experimental and theoretical results affirm that the defect-induced lattice disorders alter the electronic properties, and account for the band feature and light absorption modulation of D-HfNb₃O₈.

Figure 3a shows the H₂ evolution activity of pristine HfNb₃O₈ without disorder (0% Pd) and disorder-rich D-HfNb₃O₈ with different Pd weight ratios. Two separate light

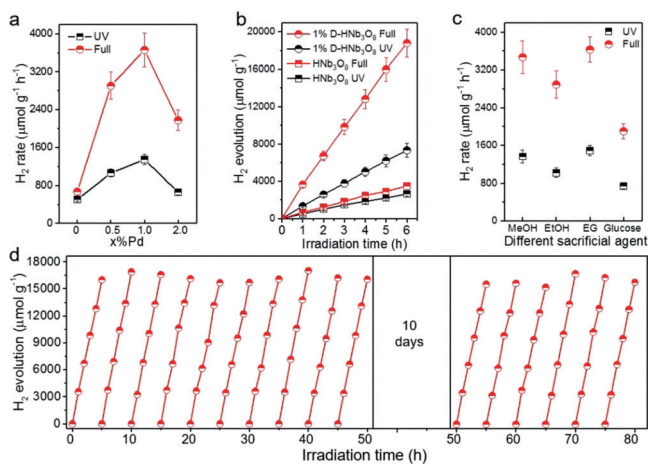


Figure 3. a,b) Photoactivity test of D-HfNb₃O₈ with different weight ratios of Pd and pristine HfNb₃O₈ (0%). c) Photoactivity test of optimal 1% Pd/D-HfNb₃O₈ with different sacrificial agents. d) Photostability test of 1% Pd/D-HfNb₃O₈. Note: MeOH, EtOH and EG refers to methanol, ethanol and ethylene alcohol, respectively.

sources of UV light (350–400 nm) and vis-NIR light ($\lambda > 400$ nm) were employed. Initially, under UV light irradiation, the D-HfNb₃O₈ displays appreciable photoactivity enhancements compared to pristine HfNb₃O₈. This can be attributed to the co-existence of abundant disorders and Pd in the material, which synergistically improve charge transportation (Figure S20) and separation (Figure S21,22). Notably, higher Pd content results in lower photoactivity. This may be ascribed to that i) high Pd loading blocks the photosensitive D-HfNb₃O₈ surface and act as recombination center,^[15] ii) high Pd content induces excessive creation of defects (Figure S23) that also act as charge recombination centers.^[16]

Subsequently, in the presence of UV light, the addition of vis-NIR light irradiation on D-HfNb₃O₈ reveals a further photoactivity enhancement. The optimal D-HfNb₃O₈ with 1% Pd displays a H₂ evolution rate of 3657 $\mu\text{mol g}^{-1} \text{h}^{-1}$, ca. 2.72 times that of D-HfNb₃O₈ under UV irradiation (Figure 3a,b). However, it is noteworthy that when the UV light is turned off, leaving just the vis-NIR light, no detectable H₂ is produced for all D-HfNb₃O₈ samples, even when the irradiation is sustained for 10 h. The finding suggests that although vis-NIR light is fully absorbed by the D-HfNb₃O₈, the supplied energy is incapable of driving the photocatalytic H₂ evolution via the classic photoexcitation of charge carriers. Also, the

result also rules out the possibility of plasmonic effect of Pd particles to induce the photoactivity enhancement. Thereby, the role of the vis-NIR light absorption by D-HNb₃O₈ is to accelerate the foregoing UV-induced photoactivity, rather than to initiate the photogenerated charge mediated catalytic reaction. Moreover, analogous photoactivity enhancement is observed for photocatalytic H₂ production with four other sacrificial agents (Figure 3c), selective reduction of 4-nitroaniline and oxidative degradation of rhodamine B (Figure S24, S25) over the D-HNb₃O₈. These results demonstrate that the vis-NIR driven photoactivity enhancement is irrespective of the reactant and reaction type. Finally, the D-HNb₃O₈ has demonstrated high photoactivity (Figure 3d) and physicochemical stability (Figure S26).

In general, extended light absorption is manipulated for supplementary catalytic activities through the generation of additional electron-hole pairs. However, in the case of the D-HNb₃O₈, this has been demonstrated to be invalid. No H₂ evolution is detected under vis-NIR irradiation, suggesting that the vis-NIR photons contribute in other way towards photoactivity improvement. Recently, heat has been demonstrated to be beneficial for photocatalysis, which is deemed to provide high kinetic energy to the photogenerated electron-hole pairs and the reactants, thereby improving the charge carriers' mobility, inhibiting their recombination and increasing the number of energetic interactions, consequently leading to enhanced photocatalytic performance.^[1b,17] In our work, the ordered structure of the D-HNb₃O₈ is retained to inherit selective high energy absorption spectrum for photoexcitation of charge carrier across its intrinsic band gap to drive photoredox activity. Whilst, the abundantly incorporated disorders generate new energy states with small band gap, which absorbs the full solar spectrum energy and converts into heat through a nonradiative thermalization process^[18] (Figure 4a). This results in a strong photothermal effect that provides localized heat to the D-HNb₃O₈-reactant complexes' proximity, and thus triggers endothermic stimulated dynamics of UV-induced charge carriers with high redox potentials to boost the reaction kinetics.

As shown in Figure 4b,c, under simulated 1 sun irradiation, the temperature of the D-HNb₃O₈ rapidly rises from 25 °C to 95 °C at 7 min. In contrast, under UV light irradiation alone, the sample shows a much less temperature increase (Figure S27), validating the significant vis-NIR light-induced heating effect. Moreover, the pristine HNb₃O₈ shows a slow temperature increment from 25 to 38 °C under the same condition (Figure 4b and S28). Additionally, the temperature evolution of the D-HNb₃O₈ reaction solution during the H₂ generation also show that under full spectrum irradiation, the temperature significantly increases from 24.4 °C to 56.4 °C (Figure S29), whereas the bare solution shows a much lower increment from 24.7 to 34.0 °C. The marked temperature increase stemming from the efficient solar-thermal conversion greatly facilitates the separation and transportation of photogenerated electron-hole pairs. It provides additional kinetic energy to the UV-excited electrons as well as holes, thereby accelerating the photoelectron-driven hydrogen evolution and the sacrificial agent-assisted hole consumption, as verified in Figure 4d-f and S30. The D-HNb₃O₈ displays

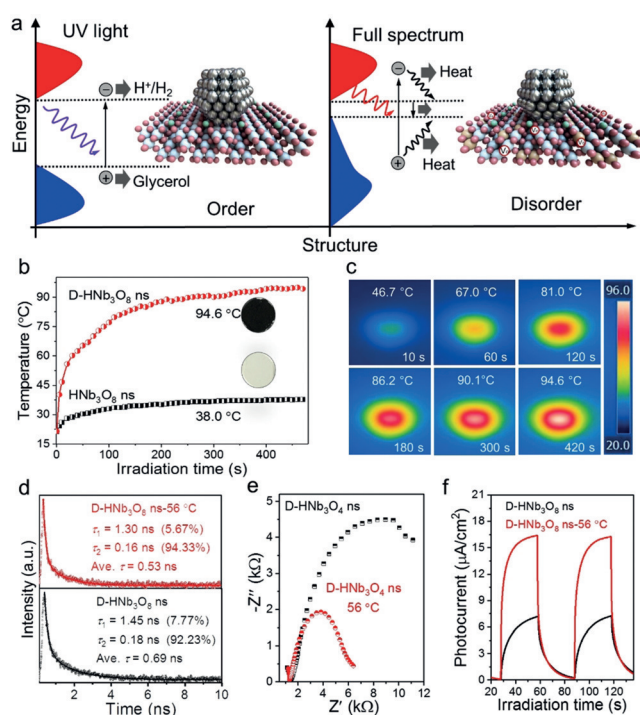


Figure 4. a) Schematic illustration of the band energies and the light absorption properties of D-HNb₃O₈. b) Temperature evolution of the D-HNb₃O₈ and HNb₃O₈, and c) infrared images of D-HNb₃O₈ under simulated 1 sun light irradiation. d) Time-resolved transient PL decay spectra, e) EIS Nyquist plots and f) transient photocurrent responses of D-HNb₃O₈ at different temperatures.

shorter average emission lifetime,^[19] lower PL intensity,^[20] smaller Nyquist semicircle^[21] and higher photocurrent^[17c] with the reaction temperature increase, which collectively reveal the inhibited charge carrier recombination, decreased interfacial charge transfer resistance as well as accelerated separation and consumption of photogenerated electron-hole pairs at higher temperature. These complementary photo- and electro-chemical analyses consolidate the thermally intensified dynamics of the charge carriers for accelerating photocatalytic reactivity.

In summary, we have demonstrated a facile approach to locally transpire lattice distortion on a crystalline monolayer HNb₃O₈, hence hybridizing ordered-disordered junction structure on ultrathin nanosheet to fulfill efficient photoredox and photothermic activation at optimal working spectrum. The as-obtained D-HNb₃O₈ realizes full solar energy harvesting from 250 to 2500 nm without trading-off its high photocatalytic activity. Specifically, the ultrathin defect-enriched “biphasic” D-HNb₃O₈ materializes high utilization of solar energy and favorable reaction kinetics to thermally promote photoredox reactivity. This approach is believed to provide a definitive avenue towards full spectrum photothermic catalysis and is expected to extend to other photocatalyst systems with tunable valence states.

Acknowledgements

This work is supported by Singapore Ministry of Education (MOE) grants (R-263-000-C85-112, R-263-000-D08-114, and R-265-000-615-114), and Singapore National Research Foundation's Competitive Research Program funding (NRR-CRP16-2015-05). The computational resources were provided by the Centre for Advanced 2D Materials, National University of Singapore.

Conflict of interest

The authors declare no conflict of interest.

Keywords: defect engineering · full solar spectrum · order-disorder · photothermic catalysis · redox reaction

How to cite: *Angew. Chem. Int. Ed.* **2019**, *58*, 3077–3081
Angew. Chem. **2019**, *131*, 3109–3113

- [1] a) G. Cui, W. Wang, M. Ma, J. Xie, X. Shi, N. Deng, J. Xin, B. Tang, *Nano Lett.* **2015**, *15*, 7199–7203; b) M.-Q. Yang, M. Gao, M. Hong, G. W. Ho, *Adv. Mater.* **2018**, *30*, 1802894.
- [2] a) H. Yu, R. Shi, Y. Zhao, T. Bian, Y. Zhao, C. Zhou, G. I. N. Waterhouse, L.-Z. Wu, C.-H. Tung, T. Zhang, *Adv. Mater.* **2017**, *29*, 1605148; b) B. Liu, J. Li, W. Yang, X. Zhang, X. Jiang, Y. Bando, *Small* **2017**, *13*, 1701998.
- [3] a) M.-Q. Yang, J. Dan, S. J. Pennycook, X. Lu, H. Zhu, Q.-H. Xu, H. J. Fan, G. W. Ho, *Mater. Horiz.* **2017**, *4*, 885–894; b) X. Liu, J. Iocozzia, Y. Wang, X. Cui, Y. Chen, S. Zhao, Z. Li, Z. Lin, *Energy Environ. Sci.* **2017**, *10*, 402–434; c) C. Li, T. Wang, Z.-J. Zhao, W. Yang, J.-F. Li, A. Li, Z. Yang, G. A. Ozin, J. Gong, *Angew. Chem. Int. Ed.* **2018**, *57*, 5278–5282; *Angew. Chem.* **2018**, *130*, 5376–5380; d) R. Shi, Y. Cao, Y. Bao, Y. Zhao, G. I. N. Waterhouse, Z. Fang, L.-Z. Wu, C.-H. Tung, Y. Yin, T. Zhang, *Adv. Mater.* **2017**, *29*, 1700803.
- [4] H. Yu, R. Shi, Y. Zhao, G. I. N. Waterhouse, L.-Z. Wu, C.-H. Tung, T. Zhang, *Adv. Mater.* **2016**, *28*, 9454–9477.
- [5] a) W. Yang, B. Liu, B. Yang, J. Wang, T. Sekiguchi, S. Thorsten, X. Jiang, *Adv. Funct. Mater.* **2015**, *25*, 2543–2551; b) K.-H. Ye, Z. Chai, J. Gu, X. Yu, C. Zhao, Y. Zhang, W. Mai, *Nano Energy* **2015**, *18*, 222–231.
- [6] Z. Zhang, J. Huang, Y. Fang, M. Zhang, K. Liu, B. Dong, *Adv. Mater.* **2017**, *29*, 1606688.
- [7] S. Liang, L. Wen, S. Lin, J. Bi, P. Feng, X. Fu, L. Wu, *Angew. Chem. Int. Ed.* **2014**, *53*, 2951–2955; *Angew. Chem.* **2014**, *126*, 2995–2999.
- [8] X. Wang, H. Shi, J. H. Kwak, J. Szanyi, *ACS Catal.* **2015**, *5*, 6337–6349.
- [9] Y. Song, H. Wang, X. Gao, Y. Feng, S. Liang, J. Bi, S. Lin, X. Fu, L. Wu, *ACS Catal.* **2017**, *7*, 8664–8674.
- [10] T. Zhang, M.-Y. Wu, D.-Y. Yan, J. Mao, H. Liu, W.-B. Hu, X.-W. Du, T. Ling, S.-Z. Qiao, *Nano Energy* **2018**, *43*, 103–109.
- [11] W. Zhang, X. Pan, P. Long, X. Liu, X. Long, Y. Yu, Z. Yi, *J. Mater. Chem. A* **2017**, *5*, 18998–19006.
- [12] a) A. Goldstein, V. Chiriac, D. Becherescu, *J. Non-Cryst. Solids* **1987**, *92*, 271–277; b) M.-Q. Yang, J. Wang, H. Wu, G. W. Ho, *Small* **2018**, *14*, 1703323; c) X. Pan, M.-Q. Yang, X. Fu, N. Zhang, Y.-J. Xu, *Nanoscale* **2013**, *5*, 3601–3614.
- [13] a) H. Liu, H. T. Ma, X. Z. Li, W. Z. Li, M. Wu, X. H. Bao, *Chemosphere* **2003**, *50*, 39–46; b) N. Shi, X. Li, T. Fan, H. Zhou, J. Ding, D. Zhang, H. Zhu, *Energy Environ. Sci.* **2011**, *4*, 172–180.
- [14] a) J. Yan, T. Wang, G. Wu, W. Dai, N. Guan, L. Li, J. Gong, *Adv. Mater.* **2015**, *27*, 1580–1586; b) J. Cai, M. Wu, Y. Wang, H. Zhang, M. Meng, Y. Tian, X. Li, J. Zhang, L. Zheng, *J. Chem. Phys.* **2017**, *146*, 084701.
- [15] O. Carp, C. L. Huisman, A. Reller, *Prog. Solid State Chem.* **2004**, *32*, 33–177.
- [16] Y. H. Hu, *Angew. Chem. Int. Ed.* **2012**, *51*, 12410–12412; *Angew. Chem.* **2012**, *124*, 12579–12581.
- [17] a) Z. Gan, X. Wu, M. Meng, X. Zhu, L. Yang, P. K. Chu, *ACS Nano* **2014**, *8*, 9304–9310; b) M. Gao, P. K. N. Connor, G. W. Ho, *Energy Environ. Sci.* **2016**, *9*, 3151–3160; c) C. K. N. Peh, M. Gao, G. W. Ho, *J. Mater. Chem. A* **2015**, *3*, 19360–19367.
- [18] J. Wang, Y. Li, L. Deng, N. Wei, Y. Weng, S. Dong, D. Qi, J. Qiu, X. Chen, T. Wu, *Adv. Mater.* **2017**, *29*, 1603730.
- [19] M.-Q. Yang, Y.-J. Xu, W. Lu, K. Zeng, H. Zhu, Q.-H. Xu, G. W. Ho, *Nat. Commun.* **2017**, *8*, 14224.
- [20] Y. Guo, J. Li, Y. Yuan, L. Li, M. Zhang, C. Zhou, Z. Lin, *Angew. Chem. Int. Ed.* **2016**, *55*, 14693–14697; *Angew. Chem.* **2016**, *128*, 14913–14917.
- [21] a) M. Ye, J. Gong, Y. Lai, C. Lin, Z. Lin, *J. Am. Chem. Soc.* **2012**, *134*, 15720–15723; b) J. Ran, B. Zhu, S.-Z. Qiao, *Angew. Chem. Int. Ed.* **2017**, *56*, 10373–10377; *Angew. Chem.* **2017**, *129*, 10509–10513.

Manuscript received: September 20, 2018

Accepted manuscript online: October 12, 2018

Version of record online: October 30, 2018